Optimising NMR Spectroscopy through Method and Software Development

Jonathan Yong

University of Oxford

Contents

refsection:1

refsection:2

Chapter 2

Pure shift NMR

Pure shift NMR refers to the technique of acquiring NMR spectra free of multiplet structure, such that every chemical environment gives rise to a singlet.[1,2] In the context of this thesis, we use the term 'pure shift' exclusively to refer to broadband homodecoupled ^{1}H spectra. Here, 'broadband' means that the couplings are removed from the entire spectrum, as opposed to just a subset of it (which can be accomplished through band-selective refocusing). 'Homodecoupled' refers to the fact that the primary target here is the removal of homonuclear couplings, which cannot be done simply through decoupling during acquisition. Finally, although pure shift techniques can be applied to any nuclide, ^{1}H spectra are of greatest interest because of the narrow chemical shift range of ^{1}H which often leads to peak overlap. (Another prominent case is ^{13}C pure shift NMR in isotopically enriched molecules, but this is not within the scope of this thesis.)

In this chapter, I first cover the theory underpinning, and a brief history of, pure shift experiments. I then describe a variety of approaches aimed at increasing the quality of pure shift experiments: this is measured both in terms of *sensitivity* as well as *purity*, i.e. the lack of spectral artefacts arising from imperfect decoupling. In all cases, we compare these against the state-of-the-art PSYCHE pure shift method.[3,4] Finally, I end with a section discussing the combination of pure shift diffusion spectroscopy—formally a pseudo-3D experiment—with the use of ultrafast (single-scan) NMR techniques to collapse the diffusion dimension. This project was carried out in collaboration with Jean-Nicolas Dumez (University of Nantes).

The work in this chapter has not been submitted for publication.

2.1 Theoretical background

In this section, I use a system with two weakly coupled spins I_1 and I_2 to illustrate the ideas behind pure shift NMR. This means that $H_{\text{free},I} = \Omega_1 I_{1z} + \Omega_2 I_{2z} + 2\pi J I_{1z} I_{2z}$; this is diagonal in

the Zeeman basis:

$$H_{\text{free}} = \begin{pmatrix} \omega_{\alpha\alpha} & 0 & 0 & 0 \\ 0 & \omega_{\alpha\beta} & 0 & 0 \\ 0 & 0 & \omega_{\beta\alpha} & 0 \\ 0 & 0 & 0 & \omega_{\beta\beta} \end{pmatrix}, \tag{2.1}$$

{eq:h_free_weak}

where $\omega_{\lambda\mu} = \langle \lambda\mu | H_{\text{free},I} | \lambda\mu \rangle$ represents the precession frequency of the state $|\lambda\mu\rangle$. Given that $I_z |\alpha\rangle = (1/2)|\alpha\rangle$ and $I_z |\beta\rangle = -(1/2)|\beta\rangle$, these are relatively easy to work out:

$$\omega_{\alpha\alpha} = \frac{1}{2}(\Omega_1 + \Omega_2 + \pi J) \quad \omega_{\alpha\beta} = \frac{1}{2}(\Omega_1 - \Omega_2 - \pi J)$$

$$\omega_{\beta\alpha} = \frac{1}{2}(-\Omega_1 + \Omega_2 - \pi J) \quad \omega_{\beta\beta} = \frac{1}{2}(-\Omega_1 - \Omega_2 + \pi J). \tag{2.2}$$

{eq:state_precessions}

The corresponding propagator for a time τ, $U = \exp(-iH_{\text{free},I}\tau)$, is then just:

$$U = \begin{pmatrix} \exp(-i\omega_{\alpha\alpha}\tau) & 0 & 0 & 0 \\ 0 & \exp(-i\omega_{\alpha\beta}\tau) & 0 & 0 \\ 0 & 0 & \exp(-i\omega_{\beta\alpha}\tau) & 0 \\ 0 & 0 & 0 & \exp(-i\omega_{\beta\beta}\tau) \end{pmatrix}. \tag{2.3}$$

{eq:u_free_weak}

In the previous chapter, we showed how pulse sequences could be analysed using two different bases for spin-½ systems, depending on which was most mathematically expedient. To analyse pure shift NMR it turns out to be most convenient to introduce a third basis, namely $\{I_\alpha, I_\beta, I_+, I_-\}$.[5–7] The definitions of these were given in eq. (1.5): it is clear from there that these represent single matrix elements of ρ when expressed in the Zeeman basis. The same is true of their products in systems containing multiple spins. Consequently, the evolution of these operators under $H_{\text{free},I}$ is extraordinarily simple to calculate in matrix form: for example, we have that

$$I_{1+}I_{2\alpha} = \begin{pmatrix} 0 & 0 & 1 & 0 \\ 0 & 0 & 0 & 0 \\ 0 & 0 & 0 & 0 \\ 0 & 0 & 0 & 0 \end{pmatrix}, \tag{2.4}$$

{eq:single_elem_plusal...}

so $U(\tau)I_{1+}I_{2\alpha}U^\dagger(\tau)$ is simply

$$\begin{pmatrix} 0 & 0 & \exp(-i\omega_{\alpha\alpha}\tau)\exp(i\omega_{\beta\alpha}\tau) & 0 \\ 0 & 0 & 0 & 0 \\ 0 & 0 & 0 & 0 \\ 0 & 0 & 0 & 0 \end{pmatrix} = \exp[-i(\Omega_1 + \pi J)\tau]I_{1+}I_{2\alpha}. \tag{2.5}$$

{eq:single_elem_plusal...}

Essentially, all of these operators evolve into themselves under $H_{\text{free},I}$, while acquiring a phase factor which depends on the difference between two of the frequencies. The rules for the single-

quantum operators on spin 1 are explicitly given here:

$$I_{1+}I_{2\alpha} \longrightarrow \exp[-\mathrm{i}(\Omega_1 + \pi J)\tau]I_{1+}I_{2\alpha} \tag{2.6}$$ {eq:shift_basis_evolut

$$I_{1+}I_{2\beta} \longrightarrow \exp[-\mathrm{i}(\Omega_1 - \pi J)\tau]I_{1+}I_{2\beta} \tag{2.7}$$ {eq:shift_basis_evolut

$$I_{1-}I_{2\alpha} \longrightarrow \exp[\mathrm{i}(\Omega_1 + \pi J)\tau]I_{1-}I_{2\alpha} \tag{2.8}$$ {eq:shift_basis_evolut

$$I_{1-}I_{2\beta} \longrightarrow \exp[\mathrm{i}(\Omega_1 - \pi J)\tau]I_{1-}I_{2\beta} \tag{2.9}$$ {eq:shift_basis_evolut

The rules for the corresponding operators on spin 2 can be easily obtained by permutation of labels. Notice that the evolution frequencies of the -1-quantum operators each correspond to one peak of the multiplet: for example, $\Omega_1 + \pi J$ and $\Omega_1 - \pi J$ (eqs. (2.8) and (2.9)) correspond to the two peaks of the spin-1 doublet.

Consider now a simple spin echo sequence, 90°_x–τ–180°_x–τ–detection. The initial excitation pulse acts on both spins 1 and 2, and thus generates a mixture of all eight possible single-quantum operators (the four above plus four more on spin 2). For simplicity, we only consider the $I_{1+}I_{2\alpha}$ term. This evolves in the first τ delay to give $\exp[-\mathrm{i}(\Omega_1 + \pi J)\tau]I_{1+}I_{2\alpha}$. The 180° pulse *flips* both spins 1 and 2, in that it causes the transitions $I_+ \leftrightarrow I_-$ and $I_\alpha \leftrightarrow I_\beta$; consequently, we have that

$$\exp[-\mathrm{i}(\Omega_1 + \pi J)\tau]I_{1+}I_{2\alpha} \longrightarrow \exp[-\mathrm{i}(\Omega_1 + \pi J)\tau]I_{1-}I_{2\beta}. \tag{2.10}$$ {eq:spin_echo_1}

In the second delay, we get a second phase factor from the evolution of the $I_{1-}I_{2\beta}$ operator:

$$\exp[-\mathrm{i}(\Omega_1 + \pi J)\tau]I_{1-}I_{2\beta} \longrightarrow \exp[-\mathrm{i}(\Omega_1 + \pi J)\tau]\exp[\mathrm{i}(\Omega_1 - \pi J)\tau]I_{1-}I_{2\beta}$$
$$= \exp(-2\mathrm{i}\pi J\tau)I_{1-}I_{2\beta}. \tag{2.11}$$ {eq:spin_echo_2}

Detection of this gives us one of the two peaks of the spin-1 doublet, as described previously, but with a phase factor tacked on. The Ω_1 terms in the phase factor are cancelled out, which reflects the fact that the offset (or chemical shift) is refocused by the 180° pulse. However, the J-evolution is not refocused, which leads to characteristic phase distortions in the detected multiplets. The same is true of all the other single-quantum operators on both spins.

In order to refocus the J-evolution as well as the chemical shift, we would need—instead of a 180° pulse—a pulse sequence element which simultaneously effects *all* of the following transitions:

$$I_{1+}I_{2\alpha} \longrightarrow I_{1-}I_{2\alpha}; \quad I_{1+}I_{2\beta} \longrightarrow I_{1-}I_{2\beta}; \quad I_{1-}I_{2\alpha} \longrightarrow I_{1+}I_{2\alpha}; \quad I_{1-}I_{2\beta} \longrightarrow I_{1+}I_{2\beta}; \tag{2.12}$$ {eq:pure_shift_require

$$I_{1\alpha}I_{2+} \longrightarrow I_{1\alpha}I_{2-}; \quad I_{1\beta}I_{2+} \longrightarrow I_{1\beta}I_{2+}; \quad I_{1\alpha}I_{2-} \longrightarrow I_{1\alpha}I_{2+}; \quad I_{1\beta}I_{2-} \longrightarrow I_{1\beta}I_{2-}. \tag{2.13}$$ {eq:pure_shift_require

Such an element forms the basis of a pure shift technique, and I refer to it here as a *pure shift element* (PSE). The difficulty in designing a PSE is that *all* spins must be simultaneously decoupled from each other (and not just one spin). For example, if we only had to invert spin 1 and not

spin 2 (i.e. only eq. (2.12) and not eq. (2.13)), this could be trivially accomplished by a selective 180° pulse on spin 1. However, this would not bring about the correct transitions for spin 2. Yet another complicating factor is that the spins will have offsets and couplings which are *a priori* not known; so the design of the PSE cannot use such parameters as inputs. These limitations mean that it is impossible to accomplish the above transitions *in full*; rather, a more realistic scenario involves

$$I_{1+}I_{2\alpha} \longrightarrow cI_{1-}I_{2\alpha} + \sum_i c'_i M_i \tag{2.14}$$ {eq:realistic_pse}

and likewise for the other operators. Here, the desired transition probability c directly correlates with the sensitivity of the PSE, and the $M'_i s$ are some other undesired operators which (if detectable) must either be suppressed or generate artefacts in the spectrum.

In the above discussion, note that the role of the PSE is to invert the I_+ and I_- terms, and to retain the I_α and I_β terms. The prevailing terminology is to refer to the spins with I_+ and I_- terms as *active spins*, and the I_α and I_β spins as *passive spins*. Thus, for example, in the context of eq. (2.12), spin 1 is active and spin 2 is passive. The detected signal always arises from the active spins.

Before moving on to the discussion of how this is accomplished in practice, I insert a slight digression about *J-resolved* (or *2DJ*) *spectroscopy*, which is very closely related to pure shift NMR. The basic 2DJ sequence involves a spin echo of duration t_1 (i.e. the τ delay above is $t_1/2$), immediately followed by detection. If we only consider a single operator and reuse the analysis above, then we have that

$$\begin{aligned} I_{1+}I_{2\alpha} &\xrightarrow{t_1/2} \exp[-\mathrm{i}(\Omega_1 + \pi J)t_1/2]I_{1+}I_{2\alpha} \\ &\xrightarrow{180°} \exp[-\mathrm{i}(\Omega_1 + \pi J)t_1/2]I_{1-}I_{2\beta} \\ &\xrightarrow{t_1/2} \exp(-\mathrm{i}\pi J t_1)I_{1-}I_{2\beta}. \end{aligned} \tag{2.15}$$ {eq:2dj_operator_analy}

This yields a complex signal of the form

$$s(t_1, t_2) = \exp(-\mathrm{i}\pi J t_1)\exp[\mathrm{i}(\Omega_1 - \pi J)t_2], \tag{2.16}$$ {eq:2dj_signal}

which when Fourier transformed yields a phase twist lineshape at $(-\pi J, \Omega_1 - \pi J)$. The other component on spin 1 (starting from $I_{1+}I_{2\beta}$) likewise yields a phase twist at $(\pi J, \Omega_1 + \pi J)$. It has long been known that *shearing* this 2DJ spectrum by 45° (i.e. moving each data point (Ω_1, Ω_2) to $(\Omega_1, \Omega_2 - \Omega_1)$) generates a spectrum which only has chemical shift information in the ω_2 dimension. After magnitude-mode processing, projection of this spectrum onto the ω_2 axis, for example, would in principle yield a pure shift spectrum.* This is true, but in practice the phase twist lineshapes cause the resulting resolution to be very poor, which defeats the purpose of using

---

*Or equivalently, projection of the unsheared spectrum along a 45° axis.[8]

a pure shift spectrum. To circumvent this issue, a glut of special processing techniques have been proposed[9–11] (see also references therein); but more ideally, we want a phase-sensitive 2DJ spectrum, where a pair of 'echo' and 'antiecho' signals are obtained:[*]

$$s_{\text{echo}}(t_1, t_2) = \exp(-\mathrm{i}\pi J t_1) \exp[\mathrm{i}(\Omega_1 - \pi J)t_2] \tag{2.17}$$

{eq:2dj_signal_ea}

$$s_{\text{antiecho}}(t_1, t_2) = \exp(\mathrm{i}\pi J t_1) \exp[\mathrm{i}(\Omega_1 - \pi J)t_2] \tag{2.18}$$

and processed in the same way as previously described in § 1.4.3 to yield the double absorption-mode lineshape. The echo signal is of course the same as in eq. (2.16), but to obtain the antiecho signal, we require a different pulse sequence with a PSE inserted right before detection. Note that we start with a different operator here, $I_{1-}I_{2\alpha}$, in order to end up with the same $I_{1-}I_{2\beta}$ operator just before detection.

$$I_{1-}I_{2\alpha} \xrightarrow{t_1/2} \exp[\mathrm{i}(\Omega_1 + \pi J)t_1/2]I_{1-}I_{2\alpha} \tag{2.19}$$

{eq:2dj_signal_antiech}

$$\xrightarrow{180°} \exp[\mathrm{i}(\Omega_1 + \pi J)t_1/2]I_{1+}I_{2\beta} \tag{2.20}$$

$$\xrightarrow{t_1/2} \exp(\mathrm{i}\pi J t_1)I_{1+}I_{2\beta} \tag{2.21}$$

$$\xrightarrow{\text{PSE}} c\exp(\mathrm{i}\pi J t_1)I_{1-}I_{2\beta}. \tag{2.22}$$

In order to apply echo–antiecho processing, the decrease in sensitivity by a factor of c must also be applied to the echo spectrum: this can be done by simply inserting the PSE before the t_1 spin echo, which does not affect the relative modulation in t_1 and t_2. Thus, we see that *exactly the same PSE* allows us to generate pure shift spectra as well as absorption-mode 2DJ spectra, a fact which has been previously demonstrated using various PSEs.[12,13] In fact, the same formalism can be used to describe a family of small flip angle COSY experiments, including ECOSY[7,14,15] and *z*-COSY;[16–18] these are also closely related to pure shift NMR. In particular, the anti *z*-COSY experiment is a precursor to PSYCHE, and is analysed in § 2.2.3. However, a full discussion of these is beyond the scope of this thesis.

2.2　Pure shift in practice

eshift__intro_practice

The previous section described the underlying theory used for analysing PSEs and showed how such an element could be used to record absorption-mode 2DJ spectra. From this, one can obtain a pure shift spectrum through shearing and projection. However, this is only an *indirect*

---

[*]The terms 'echo' and 'antiecho' refer to the relative senses of the coherences evolving during t_1 and t_2: in the echo spectrum these have opposite signs, e.g. $I_z S_+$ and I_- in the HSQC, and in the antiecho spectrum they have the same sign. As pointed out by Pell and Keeler,[12] this is not really appropriate for the 2DJ experiment since each half of t_1 has a coherence with a different sense, but we will stick to this nomenclature as the underlying concept is very similar to that of echo–antiecho processing.

route to a pure shift spectrum. In this section, we will tackle the main question of how pure shift experiments may be *directly* acquired. Following this, I cover several examples of PSEs reported in the literature. This selection is not exhaustive: I only choose to cover a handful of PSEs which *specifically* accomplish the transformations listed in eqs. (2.12) and (2.13).

2.2.1   Acquisition modes

ift__acquisition_modes

./figures/pureshift/modes.png

Figure 2.1: Possible acquisition modes for pure shift spectroscopy. The red box labelled 'PSE' indicates a generic pure shift element, which can be any of those described in the main text. In practice, gradients are also used to suppress unwanted coherence transfers; these are not shown here for simplicity. **(a)** Insertion of a J-refocusing element (JRE) in the centre of an indirect-dimension evolution period, which leads to a spectrum which is pure shift in F_1. The $90°–\tau_m–90°$ mixing period shown here is that of a NOESY experiment, but in principle it can be anything. **(b)** Real-time acquisition of a 1D pure shift spectrum in chunks of duration T_{chunk}. **(c)** Interferogram acquisition of a 1D pure shift spectrum, where t_1 is lengthened by T_{chunk} every increment.

Restating eq. (2.14), suppose we have a PSE which accomplishes the transformation

$$I_{1+}I_{2\alpha} \longrightarrow cI_{1-}I_{2\alpha} + \sum_i c_i' M_i. \qquad (2.23)$$

{eq:pse_revisited}

The simplest method of using this—and indeed, the first ever example[15]—is to insert it in the middle of a t_1 period of a 2D experiment. This is actually not entirely desirable, because the PSE causes *both* chemical shifts and J-couplings to be refocused; consequently, there will be *no* frequency modulation during t_1 at all! It is more sensible to combine the PSE with a hard 180° pulse (which refocuses only chemical shifts). Together, the effect is to refocus J-couplings and allow chemical shifts to evolve; this combination is thus called a *J-refocusing element*, or JRE (fig. 2.1a). We can equivalently say that the JRE flips all passive spins and leaves active spins untouched.

This is ideal in the sense that its implementation requires minimal modification of existing 2D experiments. Furthermore, the pure shift 'character' of the F_1 dimension may then be

mapped to the F_2 dimension through indirect covariance processing.[19–24] However, the increased resolution in the F_1 dimension provided by homodecoupling cannot really be reaped unless many t_1 increments are acquired. Furthermore, this does not help with acquiring a 1D pure shift spectrum, where there is no indirect dimension.

During direct detection, if coherences are allowed to evolve at their 'intrinsic' frequencies, no decoupling can be accomplished. In order to effectively utilise a JRE in a 1D experiment, or the direct dimension of a 2D experiment, it is necessary to periodically interrupt the acquisition and insert a JRE: this causes the chemical shift evolution to be effectively 'suspended' for the duration of the JRE, and the sense of J-evolution to be reversed (fig. 2.1b).[*] This leads to a series of FID 'chunks' which must then be concatenated to form the desired FID; the required spacing of the JREs, or equivalently the duration of each chunk T_{chunk}, must satisfy $T_{\text{chunk}} \ll 1/J$ (in practice, it is on the order of $1/(2J)$). This is referred to as real-time acquisition,[25–27] and although one still has to pay the sensitivity price of c, it allows a pure shift spectrum to be acquired in effectively the same time as the original coupled spectrum. Its 'single-scan' nature also allows, for example, the application of hyperpolarisation techniques which cannot be reproducibly repeated.[28,29]

Unfortunately, it is not always possible to perform real-time acquisition. The reason is because the JRE is applied multiple times, and each time it is, it must select for the same active and passive spins in the same molecule as it did the last time. In other words, *for any given molecule in the sample*, it must enforce this CTP:

$$I_{1-}I_{2\alpha} \xrightarrow{\text{JRE}} I_{1-}I_{2\beta} \xrightarrow{\text{JRE}} I_{1-}I_{2\alpha} \xrightarrow{\text{JRE}} I_{1-}I_{2\beta} \xrightarrow{\text{JRE}} \cdots \tag{2.24}$$ {eq:real_time_pureshif

As will be described later, the BIRD and Zangger–Sterk methods always select the same active spins in the same molecules, but the PSYCHE method notably does not. Therefore, in order to acquire pure shift PSYCHE spectra, we have to resort to the *interferogram method*, where each chunk is obtained as a separate increment of a 2D experiment (fig. 2.1c). The insertion of the JRE in the middle of the t_1 period means that when detection is started, it is 'as if' only the chemical shift has evolved for a period t_1. On each increment, one chunk—again of duration $T_{\text{chunk}} \ll 1/J$—is detected, and then t_1 is incremented by T_{chunk} so that the next chunk can be recorded. Finally, the chunks are stitched together to form the requisite FID.[†] Since the

---

[*]Relaxation during the JRE must also be taken into account for the real-time method: this causes each successive chunk to decay in intensity faster than usual, thereby leading to peak broadening, which can be an issue for very long JREs. In contrast, the interferogram method as only one JRE is applied on each increment, so the losses due to relaxation during the JRE are simply a constant factor.

[†]Not included in fig. 2.1c is the extra detail that scalar couplings are usually allowed to evolve for a period of $T_{\text{chunk}}/2$ at the start of the sequence, by the addition of a spin echo: this amounts to a *prefocusing* of J-evolution, such that J-coupling is refocused in the middle of the chunk rather than the beginning.[30] This allows chunk sizes twice as large to be used, reducing the total duration of the experiment. This J-prefocusing can also be done in a more intelligent manner via the SAPPHIRE method,[31] which is discussed in more detail in § 4.4.4.

indirect dimension is not processed by a Fourier transform, this is sometimes called a *pseudo-2D* experiment (or *pseudo-3D* if this is applied to the direct dimension of a 2D experiment, and so on). In this case, the sensitivity drop c is incurred, but there is on top of that also a time penalty in that the experiment duration must be lengthened by n times in order to collect n chunks. n is typically on the order of 16–32.

2.2.2 Pure shift elements

Figure 2.2: A selection of pure shift elements. **(a)** Zangger–Sterk PSE,[32] involving the combination of a selective 180° refocusing pulse and a weak gradient. **(b)** BIRD PSE;[33,34] the delay Δ is set to $1/(4 \cdot {}^1J_{CH})$. **(c)** Time-reversal PSE,[15] simply consisting of a hard pulse with variable flip angle β. Multiple spectra with different values of β must be co-added to suppress artefacts (though not completely, as discussed in the text). **(d)** PSYCHE PSE,[3] consisting of two saltire pulses[4,35] with flip angle β, and a weak gradient.

We are finally now in a position to describe individual PSEs and their mechanism of action. We begin with the Zangger–Sterk (ZS, or 'slice-selective') PSE,[32] where a selective refocusing pulse and a weak gradient are simultaneously applied (fig. 2.2a). In practice, an rSNOB pulse[36] is often used as the refocusing pulse. The effect of the gradient is to make each spin in the sample have a spatially dependent offset; conversely, since the the refocusing pulse has a specific, narrow, bandwidth, in each *slice* (or cross-section) of the sample a different spin will fall within this bandwidth. This spin is refocused by the PSE and therefore becomes the active spin *within that specific slice*; the bracketing pair of CTP gradients serve to destroy coherences on all the other spins which are not inverted. Each signal of the pure shift spectrum therefore derives from a specific slice of the sample; during direct detection, all slices simultaneously contribute to the signal, thus yielding a broadband pure shift spectrum.

The sensitivity of the ZS method tends to be low (the factor c tends to be on the order of ~ 0.01 to 0.05), as each signal only derives from a narrow region of the sample. Nevertheless, it still finds wide usage in pure shift applications nowadays, especially because it is compatible with the real-time acquisition mode:[26] as long as the pulse and the weak gradient are the same each time, then the same active spins will always be chosen in the same slice (as long as diffusion effects are ignored). The PSE can also be customised through the bandwidth of the refocusing pulse: decreasing this improves the spatial differentiation between spins which have similar intrinsic offsets, yielding better decoupling quality, albeit at the cost of sensitivity. The ZS element can be easily—and has been—adapted for use in many experiments, including (but not limited

to) absorption-mode 2DJ spectroscopy[12] and selective refocusing (SERF) experiments for the measurement of $^nJ_{HH}$.[37–40]

Next up is the *bilinear rotation decoupling* (BIRD) pulse element (fig. 2.2b). BIRD is not spatially selective like the ZS method; instead, it is *isotope-selective* in that it acts as a 180°_y pulse on ^{13}C–bound protons, and does not affect ^{12}C–bound protons. Consequently, all ^{13}C–bound protons become the active spins in the context of pure shift NMR. The first report of the BIRD element,[33] in 1982, was clearly ahead of its time: it reported the use of an interferogram-type approach to obtain 1D pure shift spectra. However, in the subsequent decades, this seemed to have been forgotten: BIRD found much more use as an isotope-selective rotation element in heteronuclear NMR,[41] until its use as a pure shift element was 'rediscovered'.[34,42]

An immediate drawback of BIRD is that it does not decouple geminal (diastereotopic) CH_2 groups, as both protons would be either both active or both passive. The sensitivity penalty of BIRD is also relatively severe: the factor c derives from the natural abundance of ^{13}C, which is approximately 0.011. However, it is also compatible with real-time acquisition,[25] and has found particular success as a pure shift element in the F_2 dimension of HMQC and HSQC experiments:[27,42–46] in this case, the use of BIRD leads to no loss of sensitivity as only ^{13}C–bound protons are detected in HSQC experiments anyway.[*] It should be noted that the BIRD element does not need to be combined with a hard 180° pulse to form a JRE: the inverse effect of only flipping the passive spins can be accomplished by simply changing the phase of both internal 180° pulses to $+y$. Using the nomenclature of Uhrín et al.,[41] the PSE and JRE forms of the BIRD pulse can be labelled as BIRD^{d,X} and BIRD^{r,X} respectively.

The *time-reversal* PSE (fig. 2.2c) is even simpler: it consists only of one hard pulse with flip angle β.[15] The catch is that the experiment must be repeated with different values of β, and the results added up with specific weightings.[7] This leads to cancellation of *some*, but not all, of the unwanted coherences: for example, on its own, it does not suppress COSY-type coherence transfer such as $I_{1-}I_{2\alpha} \to I_{1\alpha}I_{2+}$. This proved to be inconsequential in the original application of F_1 decoupling in a 2D NOESY;[15] however, it is not acceptable in a 1D context as it leads to substantial artefacts. This will be discussed in more detail in § 2.5, so a fuller analysis of the time-reversal PSE is deferred until then.

Finally, we come to the PSYCHE method, which is generally considered the current state of the art for pure shift NMR.[3] The corresponding PSE consists of two swept-frequency pulses applied during a weak gradient: for example, a pair of chirps with opposite sweep directions can be used. Using two *saltire pulses*, pulses which simultaneously sweep in both directions, leads to an increased signal-to-artefact ratio.[4] The operation of this PSE is not easy to fully explain.[35] However,

---

[*]In fact, the sensitivity is increased by the collapse of multiplet structure.

we can adopt the (not fully accurate, but still useful) instant-flip approximation[47,48]—that the swept-frequency pulse acts as an instantaneous 180° rotation on each frequency it passes through. Using this, the PSYCHE element (or strictly, the PSYCHE JRE, including a hard 180° pulse) may be viewed as a spatially parallelised version of the anti z-COSY experiment,[16,17] which we now describe.

2.2.3 PSYCHE in detail

Figure 2.3: A closer look at the mechanism of the PSYCHE PSE. (**a**) The β–z-filter–β mixing period used in the original anti z-COSY experiment. This has a similar action to a JRE, but does not suppress COSY-type coherence transfers from spin i to spin j. (**b**) An illustration of how COSY-type artefacts are suppressed by the PSYCHE pulse element. The desired CTP which remains on spin 1 is rephased by the gradients, but the COSY CTP is dephased. (**c**) An illustration of how zero-quantum terms are suppressed by the PSYCHE element through spatial averaging: in each slice of the sample (highlighted in blue and orange), the zero-quantum terms are allowed to evolve for a different duration.

The anti z-COSY experiment utilises a β–z-filter–β mixing period (fig. 2.3a), where β is a small angle, typically 10° to 20°. The role of the z-filter[49] is to remove zero-quantum terms such as $I_{1-}I_{2+}$ between the two β pulses, retaining only population terms such as $I_{1\alpha}I_{2\alpha}$. In an elegant paper by Pell et al.,[17] it was shown that by isolating the diagonal peaks of a 2D anti z-COSY experiment and taking the 45° projection of these, a pure shift spectrum could be obtained. Here, we will go one step further and consider the *direct* use of this element as a JRE: this will reveal problems which are circumvented by the PSYCHE experiment.

An analysis on a two-spin system (see Pell et al. for the equivalent analysis on a three-spin system) shows that this element converts the term $I_{1+}I_{2\alpha}$ to

$$I_{1+}I_{2\alpha} \longrightarrow \underbrace{\frac{1}{2}S^2c^4I_{1+}I_{2\beta}}_{\text{term 1}} + \underbrace{S^2c^2s^2I_{1+}I_{2\alpha}}_{\text{term 2}} - \underbrace{\frac{1}{4}S^2c^4I_{1\alpha}I_{2+} + \frac{1}{4}S^2c^4I_{1\beta}I_{2+}}_{\text{terms 3 and 4}} + \cdots, \qquad (2.25)$$

where $S = \sin\beta$, $s = \sin(\beta/2)$, and $c = \cos(\beta/2)$. Other terms with different coherence orders have been neglected (on the basis that they can be easily suppressed with bracketing CTP

gradients), and terms with higher orders in s have been discarded since $s = \sin(\beta/2) \ll 1$ for small β.

The first term $I_{1+}I_{2\beta}$, corresponding to the flipping of passive spins only, is the only term we want to see from a JRE. The second term, $I_{1+}I_{2\alpha}$, corresponds to the case where neither active nor passive spins have been flipped. In the original anti z-COSY work, these give rise to 'off-diagonal' peaks which are part of a multiplet on the diagonal, but when projected at 45° generate artefacts around the pure shift peak. In the context of pure shift NMR, these are called 'recoupling artefacts', as they arise from imperfect J-refocusing. Note that the ratio of recoupling artefacts to desired signal is proportional to $S^2c^2s^2/S^2c^4 = \tan^2(\beta/2)$: using a smaller value for β therefore leads to better signal-to-artefact ratios, but also lower overall sensitivity. The PSYCHE element is similar to the β–z-filter–β element in this regard: it does not suppress the recoupling artefacts, but instead relies on the user choosing a suitable value for β such that the artefact-to-signal ratio is tolerably small. If the sensitivity proves to be insufficient, the flip angle β may be increased instead: this leads to a larger artefact-to-signal ratio, but if the sample is not concentrated anyway, it may well be that the artefacts do not rise above the noise level.

The third and fourth terms, $I_{1\lambda}I_{2+}$ ($\lambda \in \{\alpha, \beta\}$), represent 'COSY-type' coherence transfer to a coupled spin: these led to crosspeak multiplets in the original anti z-COSY, which could be removed by hand before taking the projection. However, in a pure shift sequence, the peaks arising from these terms cannot simply be removed in the same way. It is precisely this issue which precludes the β–z-filter–β element from being directly used as a JRE, and motivates the development of the PSYCHE PSE, which *does* suppress these coherence transfers.

To understand how this occurs, we invoke the instantaneous spin-flip assumption. Each coherence I_{i+} is converted (or 'flipped') to a population term $I_{1\lambda}$ at a specific point $\alpha\tau_p$ after the start of the first chirp, and can be reconverted to a coherence on the same spin I_{i-} at a time $\alpha\tau_p$ before the end of the second chirp (the green CTP in fig. 2.3b).[*] Here, τ_p is the duration of the chirp and $0 < \alpha < 1$. In this case, the coherence is perfectly rephased by the weak gradient applied during the chirp pulses, since the *time* it experiences these gradients for is the same on both sides of the chirps. Now, if the I_{i+} term is converted to a coherence on a different spin I_{j-}, it experiences the gradient for a total duration of $\alpha\tau_p$ after the start of the first chirp, and also $\alpha'\tau_p$ before the end of the second chirp (the red CTP in fig. 2.3b). In general, $\alpha \neq \alpha'$ as spins i and j have different offsets; therefore, this CTP is dephased by the gradients, resulting in complete suppression of the COSY-type artefacts in the spectrum.

It remains to also consider how the PSYCHE element selects for the population terms between the two spin flips. Any terms with nonzero coherence order are simply dephased by the weak

---

[*] Note the change in the sign of the coherence, which differs from the analysis of the anti z-COSY experiment. This arises because we are only considering the PSYCHE PSE on its own, *not* the JRE.

gradient. However, zero-quantum terms (in homonuclear systems) are not dephased by gradients, and to eliminate them in a single-scan manner, they must be spatially averaged: this is what the *z*-filter in the anti *z*-COSY does, for example. It turns out that the PSYCHE element also does a similar spatial averaging. Following on from the previous paragraph, the time *between* the spin flips (for the desired pathways, i.e. not COSY-type coherence transfer) is given by $2(1 - \alpha)\tau_\mathrm{p}$. At the same time, the weak gradient induces a range of offsets across the sample, much like in the Zangger–Sterk experiment. Thus, the offset, and thus the value of α, for a given spin depends on which slice it is in; for example, fig. 2.3c uses values of α_1 and α_2 for two different slices (blue and orange). If zero-quantum terms are present between the spin flips, they evolve during this time and accrue a spatially-dependent phase: summation of these during FID acquisition leads to a cancellation of these terms. Only population terms such as $I_{1\alpha}I_{2\alpha}$ survive during this, as they do not precess during this time.

The sensitivity of PSYCHE is significantly better than for other methods: depending on the flip angle β chosen, c is typically on the order of 0.05–0.15 (see also fig. 2.4 for explicit simulations). Furthermore, it is generally more robust with respect to strong coupling compared to other pure shift methods (artefacts from strong coupling often arise due to unexpected coherence transfer,[6] which is suppressed in a similar way to the COSY-type artefacts). These two factors alone have meant that PSYCHE has enjoyed substantial adoption since its introduction: a large number of 2D experiments utilising PSYCHE decoupling in either F_1 or F_2 have been developed,[24,50–55] notably the PSYCHE-iDOSY diffusion experiment,[56] where the increased resolution provided by pure shift spectroscopy translates into increased resolution in the *diffusion* dimension as well. Like the ZS element before it, the PSYCHE element has also been used for the acquisition of absorption-mode 2DJ spectra.[13]

Despite this success, PSYCHE suffers from one significant drawback: it cannot be used in a real-time fashion. The PSYCHE PSE is often said to select active and passive spins in a 'statistical' manner: this is because of the c^2 and s^2 terms arising from the low-flip angle pulses. What this really means is that we do not care *exactly* which spins are active and which are passive, but that a certain proportion of the spins are active and passive. Repeated application of the PSE therefore does not select for the same active spins each time, which precludes its application to real-time acquisition.

Although the PSYCHE PSE may appear deceptively simple at first glance, the closer analysis given here (and elsewhere[4]) clearly shows that its inner workings are anything but. Along with other ingenious experiments such as the *z*-filter,[6] ultrafast NMR,[57–59] and more recently GEMSTONE,[60] PSYCHE is a prime example of how *spatiotemporal averaging* and pulsed field gradients can be used to great effect in modern NMR spectroscopy.[61]

At the same time, PSYCHE itself is not *perfect*: it does not fully suppress recoupling artefacts,

and can only be used in the interferogram mode. To improve on PSYCHE would therefore entail one of the following:

1. increasing the sensitivity (while maintaining purity);

2. increasing the purity (while maintaining sensitivity); or

3. developing a pure shift element which is compatible with real-time acquisition while giving comparable sensitivity and purity to PSYCHE.

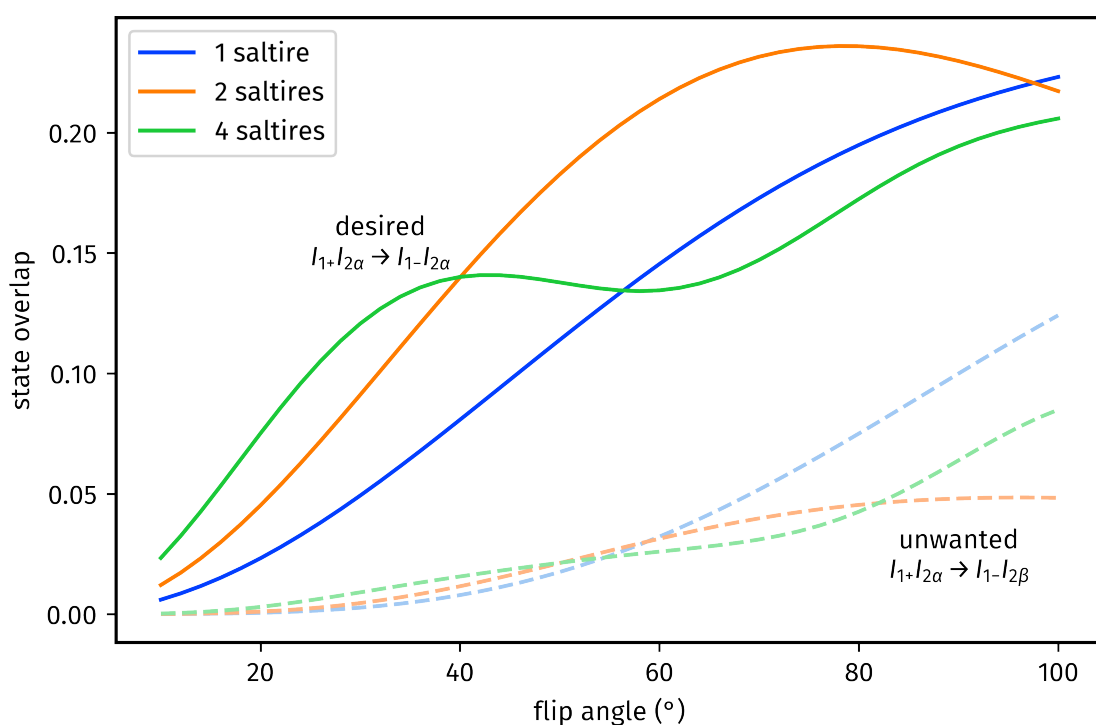The sections which follow describe my efforts towards objectives (1) and (2).

2.3 PSYCHE with a variable number of saltires

sec:pureshift__nsaltire

fig:fa_dependence_124

Figure 2.4: Simulated signal and artefact intensity for various PSYCHE-style PSEs as a function of the flip angle used. Calculations were performed on a two-spin system with a coupling of 7 Hz, and an offset difference of 1.5 kHz. The total PSE duration was 30 ms (so, for example, in the four-saltire PSYCHE, each saltire was 7.5 ms). Solid lines indicate the coefficients for the desired $I_{1+}I_{2\alpha} \to I_{1-}I_{2\alpha}$ pathway which contributes to the pure shift signal; dashed lines the coefficients for the undesired $I_{1+}I_{2\alpha} \to I_{1-}I_{2\beta}$ pathway, which gives rise to recoupling artefacts.

The first attempted method was to change the number of saltire pulses used in the waveform. As described above, PSYCHE relies on spatiotemporal averaging to suppress unwanted artefacts: this crucially relies on the fact that the pulse(s) used in the PSE are symmetric. This can be accomplished with two opposing chirps, or two saltires, both of which are symmetric. However,

a *single* saltire is also symmetric in itself: it is not hard to show that the analysis given in § 2.2.3 is still valid for a single saltire. Likewise, the use of four saltires would also be valid.

Theoretical simulations show that the overall profile of signal and artefact versus flip angle (unsurprisingly) varies with the number of saltires: in particular, using more saltires with a smaller flip angle generally accomplishes a similar effect (fig. 2.4). This may be qualitatively rationalised as more saltires providing more possible CTPs which generate the desired signal (the same idea is generally invoked when discussing the difference between unidirectional chirps and saltires[4]). However, regardless of the number of saltires, the fundamental strategy of adjusting the flip angle to control the signal-to-artefact ratio remains valid, which naturally raises the question of whether specific pulse parameters can be chosen in order to obtain the best decoupling quality.

Figure 2.5: **(a)** The peak in the pure shift spectrum of andrographolide used for calculation of signal and artefact intensity. The recoupling artefacts flanking the main peak are clearly visible. **(b)** Peak heights of the desired signal (the central peak) and artefacts (the mean of the two flanking peaks), as a function of flip angle. **(c)** Quadruple-saltire PSYCHE with $\beta = 55°$. **(d)** The reference spectrum, a double-saltire PSYCHE with $\beta = 20°$. The peak at 3.85 ppm used for the sensitivity and purity analysis is labelled with an arrow. *Data code:* `7A-201016`.

We first consider the quadruple-saltire PSYCHE. In the first instance, we set the total duration of

the PSE to 30 ms: this implies that each saltire is 7.5 ms long. For this experiment, the sensitivity was defined as the maximum height of the main peak in fig. 2.5a, and the artefact as the mean of the maximum heights of the two artefacts surrounding it. The plot in fig. 2.5b shows how these quantities vary as a function of the flip angle. Interestingly, for the artefacts, the profile observed is similar to that in the simulations: the double-saltire version performs better at low and very high flip angles, but in the middle there is a region where the quadruple-saltire version has lower artefact intensity. The signal intensities for both the double- and quadruple-saltire versions, however, seem to plateau off rather more quickly than the simulations suggest.

To highlight one particular data point, fig. 2.5b suggests that the quadruple-saltire experiment with $\beta \approx 55°$ has a similar artefact level to the double-saltire experiment with $\beta \approx 20°$, but with substantially greater signal intensity. Insets from these two spectra are respectively shown in figs. 2.5c and 2.5d. In fact, this conclusion seems to be true for the peak in question, which is at the right edge of the spectral insets shown here. Overall, the quadruple-saltire 55° experiment does have better sensitivity than the double-saltire 20° experiment. However, the artefact intensity is not always suppressed as nicely as it is in the chosen reference peak: for example, the peak at 4.05 ppm is significantly less clean in the quadruple-saltire experiment. Any apparent advantage over the double-saltire experiment is therefore not very clear—at least from this data alone.[*]

Moving on to the single-saltire case, in addition to searching for a better signal and artefact profile, another possible motivation would be that the duration of the PSE can be decreased. This would minimise losses due to relaxation and diffusion during the PSE, which were not taken into account in fig. 2.4 (and the simulations there did not vary τ_p anyway). A single-saltire PSYCHE experiment was thus recorded with various combinations of flip angle ($\beta/° \in \{15, 20, 25, 28, 30\}$) and pulse duration ($\tau_p/\text{ms} \in \{15, 25, 30, 35, 45, 55\}$). In a similar way to the quadruple-saltire study, the sensitivity here was defined as the maximum height of the main peak in fig. 2.6a, and the artefact as the mean of the heights of the two artefacts surrounding it. (However, note that the compound used was different.) The purity, or signal-to-artefact ratio, is simply the former divided by the latter.[†]

The results thus obtained are shown in fig. 2.6b. In this plot, both the sensitivities as well as the signal-to-artefact ratios are normalised with respect to the reference double-saltire experiment (black dot at (1, 1), acquired using $\beta = 20°$ and a total $\tau_p = 30\,\text{ms}$, i.e. 15 ms per saltire). An

---

[*]In fact, I also performed some preliminary experiments where the four-saltire PSE was lengthened to 60 ms. The artefact behaviour in these spectra were better than in their 30 ms counterparts, which is to be expected since a longer PSE leads to better spatiotemporal averaging. However, I unfortunately did not compare these against a 60 ms double-saltire experiment, so these results are not included in this thesis. (It would be rather unfair to compare them against the 30 ms double-saltire.)

[†]As an alternative, the Bruker `sinocal` AU programme was also used to measure the sensitivity of the spectrum; it yielded extremely similar results, so is not shown here. I found the `sinocal` routine to be rather unreproducible as the exact value calculated depends on random noise.
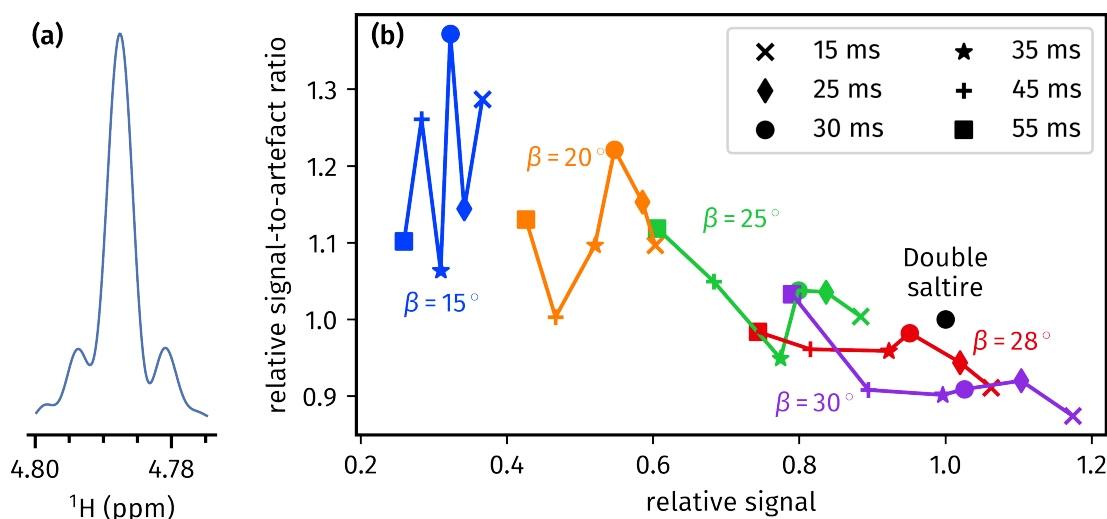
Figure 2.6: **(a)** The peak in the (reference, double-saltire) pure shift spectrum of cyclosporin used for calculation of signal intensity and signal-to-artefact ratio. **(b)** Plot showing the signal intensity and signal-to-artefact ratio obtained in various single-saltire PSYCHE experiments, normalised against the double saltire experiment with $\beta = 20°$ and $\tau_p = 30$ ms. Each line represents a series of single-saltire experiments acquired with the same value of β; τ_p generally decreases going left to right (i.e. a longer pulse means less signal). *Data code:* `5C-190617`.

ideal PSE would fall in the top-right corner of this plot. Clearly, as the flip angle increases, the sensitivity increases but at the cost of the purity: this is hardly unsurprising given that the double-saltire experiment has the same property.

While there is no standout candidate which is *clearly* better than the double saltire (i.e. greater sensitivity as well as purity), the single-saltire pulse with $\beta = 28°$ and $\tau_p = 30$ ms comes close in performance to the double-saltire experiment. (The use of $\beta = 28°$ here is not coincidental: this flip angle for a single saltire was chosen to (approximately) match the sensitivity of the $\beta = 20°$ double-saltire experiment.) It is generally true that a shorter PSE yields to increased signal, and that usable results were obtained even with a simple 15 ms saltire. However, a shorter PSE also leads to poorer spatiotemporal suppression of artefacts depends and thus poorer purity.

Both the single- and quadruple-saltire cases suffer from the classic dilemma of pure shift NMR: just as in the original PSYCHE, and in the Zangger–Sterk method before it, there is a compromise between sensitivity and purity, and one can only be increased at the cost of the other. Arguably, then, there is not much value in changing the number of saltire pulses as simply varying the *flip angle* of the basic double-saltire already gives the experimentalist a way to balance these competing objectives.

2.4 Direct optimisation of PSYCHE waveform

ureshift__optimisation

The changes to the PSYCHE waveform discussed in the previous section—changing the number of saltire pulses to either 1 or 4—are fairly minor, in that they do not fundamentally alter the form of the PSE. Furthermore, there is an obvious issue in that the quality of the spectrum is not measured in a particularly rigorous manner. Ideally, we would like to have a mathematical way of measuring how well the pure shift sequence has worked. Such a metric would also enable a more automated optimisation process, where a programme is allowed to find the best PSE without any interference from human subjectivity.

In this section, I discuss more radical changes which depart from the tried-and-tested saltire pulse. I also show how two different *cost functions*—functions which determine how 'bad' a spectrum is—can be used to evaluate PSEs. Although the work in this section did not quite yield any groundbreaking results, it provided substantial insights into the nature of pure shift optimisations, which were later used in the context of POISE (chapter 3).

2.4.1 Techniques for pure shift optimisations

hift__optim_techniques

Throughout this chapter (and more generally this thesis), various algorithms are used for *optimisation*: that is, to find the parameters $\mathbf{x} \in \mathbb{R}^n$ which minimise a *cost function $f : \mathbb{R}^n \to \mathbb{R}$*. The theory of optimisation is covered in more detail in § 3.1, so will not be repeated now. Here, I make a distinction only between *derivative-based* and *derivative-free* optimisation algorithms: the former use extra information in the form of ∇f to help locate the optimum, whereas the latter do not, using only the value of $f(\mathbf{x})$. While derivative-based algorithms typically converge to an optimum more quickly, they are unsuitable for problems where the cost function f is noisy. In this section, the Nelder–Mead (NM) simplex algorithm[62] was used: it is a very popular derivative-free method, and although mathematical convergence is not guaranteed,[63] in practice such cases are rather unlikely to arise. In this section, the implementation of the NM algorithm in the Python `scipy` package was simply used as-is.

The cost function measuring the performance of a pure shift experiment can be measured in one of two ways: either *theoretically*, in that the pure shift experiment is simulated using the density operator formalism, or *experimentally*, in that the experiment is run on a spectrometer. Unfortunately, the simulation of PSYCHE-type PSEs, where a shaped pulse is applied together with a gradient, requires a large amount of time. The pulse itself already has $n \sim 10000$ points, but on top of that, the application of gradients also requires splitting up the sample into multiple slices (often 100 to 1000) such that the evolution of ρ can be simulated in each slice and the results

summed up. To make matters worse, H_{pulse} does not commute with H_{grad}, so a propagator

$$U(i, z) = \exp\left[-i(H_{\text{grad}}(z) + H_{\text{free}} + c_x^{(i)}I_x + c_x^{(i)}I_y)(\delta t)\right] \tag{2.26}$$

{eq:pulse_gradient_pro

must be calculated for each pulse point ($1 \leq i \leq n$) in each slice of the sample. As a result, the simulation of PSYCHE spectra in the Spinach package[64] typically requires minutes to hours.[*]

This in fact makes it faster to experimentally acquire a pure shift spectrum and calculate a cost function based on that. Running an actual pure shift experiment, though, is suboptimal: firstly, the pseudo-2D interferogram method is slow, and secondly, there is no easy way to devise a cost function for the resulting spectrum. Instead, we can use a simple 1D 'pure shift spin echo' (PSSE) sequence, which has the form 90°–τ–PSE–τ–detect (fig. 2.7b). An ideal PSE would lead to complete refocusing of both chemical shifts and J-couplings, and the signal detected after this would simply be the same as in a pulse–acquire experiment (fig. 2.7a). Of course, there is a sensitivity penalty which reflects that of the PSE. On top of that, if the J-refocusing is not perfect, then the multiplets in the spin echo sequence acquire a degree of phase distortion: the delay τ has to be long enough to allow for this, but its exact value is otherwise largely insignificant. These distortions are just about visible in fig. 2.7b.

./figures/pureshift/psse.png

Figure 2.7: **(a)** Pulse–acquire experiment and the resulting spectrum. **(b)** Pure shift spin echo experiment and the resulting spectrum. The PSE used was the PSYCHE double saltire, with a flip angle of 25°; the delay τ was 11 ms. The OH peak at 4.1 ppm is lost, most likely due to chemical exchange. *Data code:* 6A-200816.

---

[*]With highly optimised handwritten code, exploiting the symmetry of the PSYCHE element, the fastest simulation I could do took 16 seconds on a 20-core computer. It is possible that GPU acceleration could result in substantial speedups, but I have not looked into this sufficiently. Anyway, acquisition of the pure shift spin echo experiment takes only around 5 seconds.

Two cost functions were designed and used in this section:

$$f_{\text{phase}} = \text{Var}_i \left[\arctan \left(\frac{S_{\text{re},i}}{|S_{\text{im},i}|} \right) \right] \tag{2.27}$$
{eq:ps_cf_phase}

$$f_{\text{diff}} = \left\| \frac{\mathbf{S}_{\text{re}}}{\|\mathbf{S}_{\text{re}}\|} - \frac{\mathbf{T}_{\text{re}}}{\|\mathbf{T}_{\text{re}}\|} \right\|, \tag{2.28}$$
{eq:ps_cf_diff}

where the PSSE and pulse–acquire 1D spectra are treated as complex-valued vectors $\mathbf{S}$ and $\mathbf{T}$ respectively (for *'spectrum'* and *'target'*). S_{re} and S_{im} are the real and imaginary parts of the spectrum $\mathbf{S}$, and $S_{\text{re},i}$ is the i-th point of the real part of the spectrum. The operator Var_i represents the variance over all points in the spectrum i, and $\|\mathbf{x}\|$ denotes the 2-norm of the vector $\mathbf{x}$, i.e. $\sqrt{\sum_i x_i^2}$. The implementation of this in Python is quite possibly easier to take in:[*]

```python
import numpy as np
# assume S and T are complex numpy arrays which have been read in
Sr = np.real(S); Si = np.imag(S); Tr = np.real(T)
f_phase = np.var(np.arctan(Sr / np.abs(Si)))
f_diff = np.linalg.norm((Sr / np.linalg.norm(Sr)) - (Tr / np.linalg.norm(Tr)))
```

These two cost functions were chosen as they exhibited desirable characteristics on synthetic data (fig. 2.8). Here, the 'target' spectrum was chosen to simply be an in-phase absorption-mode doublet with an SNR of 500. Synthetic data with increasing amounts of phase distortion (i.e. spectra ranging from in-phase absorption, to antiphase dispersion) were generated, and extra Gaussian noise added to create different SNRs. It can be seen that, for data which is well-phased (left edges of the plots), both f_{phase} (fig. 2.8a) and f_{diff} (fig. 2.8b) penalise lower SNRs. Furthermore, both of the cost functions penalise phase distortions in multiplets, since they increase going left to right. This penalty is stricter for high-SNR spectra, which is also desirable, since it is only in high-SNR spectra that the phase distortions become noticeable.

The cost function f_{diff} is easier to comprehend: it simply scales both the target and PSSE spectra down by their respective intensities, and compares each point to determine whether the peak shapes obtained are similar. Although this seems like it should be agnostic towards signal intensity, this is only true for noiseless spectra. If a (genuine) PSSE spectrum has low SNR, $\|\mathbf{S}_{\text{re}}\|$ will be small, and the noise will be scaled down less than for the target spectrum; this difference in the noise then contributes towards the cost function. On the other hand, a proper rationalisation of why the cost function f_{phase} works is unfortunately not within my capabilities! It was mostly developed by trial-and-error, and I do not have a good explanation of why it has the properties describe above.

---

[*]The use of `np.arctan` (the arctangent), and *not* `np.arctan2` (the argument of a complex number), is intentional. The behaviour shown in fig. 2.8 isn't reproduced with `arctan2`. Of course, this means the name 'phase' is a misnomer; it's not really the phase of anything meaningful.
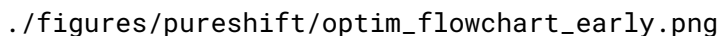
./figures/pureshift/fa_scan_synthetic.png

Figure 2.8: Behaviour of the two cost functions, f_{phase} and f_{diff}, on synthetic spectra with various SNRs. Zero phase distortion refers to an in-phase absorption-mode doublet, whereas complete phase distortion refers to an antiphase dispersion-mode doublet. **(a)** The f_{phase} cost function. **(b)** The f_{diff} cost function, measured against a spectrum with no phase distortion and an SNR of 500.

The general optimisation procedure is conceptually simple and largely consists of the loop shown in fig. 2.9: this is essentially a specialised version of the POISE flowchart (CREF TO FIG). The optimisation algorithm is responsible for determining convergence, as well as choosing the new parameters based on previously obtained information; the initial parameters must be supplied by the user.

In practice, it is a technical challenge to implement this loop on a spectrometer as the cost function calculation is performed either in Matlab or Python 3, both of which are not compatible with Bruker's TopSpin software. TopSpin instead provides Jython (Python 2.7) and C programming interfaces;[*] the former is not compatible with Python 3 packages like `numpy` or `scipy`, and the latter is too low-level to be worth implementing numerical algorithms in.[†] Thus, we require a means of *communication* between the spectrometer and the optimisation control programme: this includes a signal from the controlling programme to trigger acquisition on the spectrometer, as well as a signal from the spectrometer that acquisition is done so that the cost function can

---

[*]TopSpin 4.1.4 introduced a Python 3 interface which would have made much of this work simpler. Unfortunately, this was not available at the time of this work.

[†]Of course, heavily optimised code in low-level languages such as C and Fortran—or perhaps even Matlab— would run faster. However, speeding up the code has virtually no impact on the optimisation, since its rate is limited by spectrum acquisition. In this situation, it makes far more sense to save *developer time*.

./figures/pureshift/optim_flowchart_early.png

:optim_flowchart_early

Figure 2.9: Flowchart illustrating the steps for optimisation of a pure shift spectrum.

be calculated. As it turns out, the code used for the optimisations in this section was a very rudimentary and fragile form of that eventually used in POISE (for example, the aforementioned signals were transmitted via the creation and deletion of files). I therefore defer the discussion of this issue to § 3.2, where the more robust POISE interface is explained in detail.

2.4.2   Flip angle optimisation

ubsec:pureshift__faopt

Having described the rest of the optimisation setup, it remains to choose exactly which parameters are subjected to optimisation. The simplest option is to only optimise one parameter, namely the flip angle of the (double-)saltire pulse. The flip angle dependence of PSYCHE spectra is well-understood, which crucially allows us to evaluate the cost functions outlined above and determine whether they are functioning correctly.

I first sought to measure how the cost functions described above varied with the flip angle. To this end, pure shift spin echo spectra using a *single* saltire as the PSE and various flip angles (from 4° to 50°) were acquired. Since both cost functions penalise both low sensitivity and low purity, we expected that there would be an intermediate value where neither sensitivity nor purity were penalised too much: this would the optimum to seek. In the event, it was found that only f_{diff} yielded a useful minimum at around 30° (albeit only a very shallow one, fig. 2.10).

- Explain 'why' the two cost functions work (we can only really explain it for specdiff, not phase)

- Note that specdiff works almost by coincidence — why does it have that exact balance of sensitivity vs purity? It could easily be something else. Note that this has not much relation to quality of pure shift spectra.

- Briefly mention that optimisations were done and converged to minimum as shown in plot — no need to go into ynamide optimisations as the 70° result is dubious
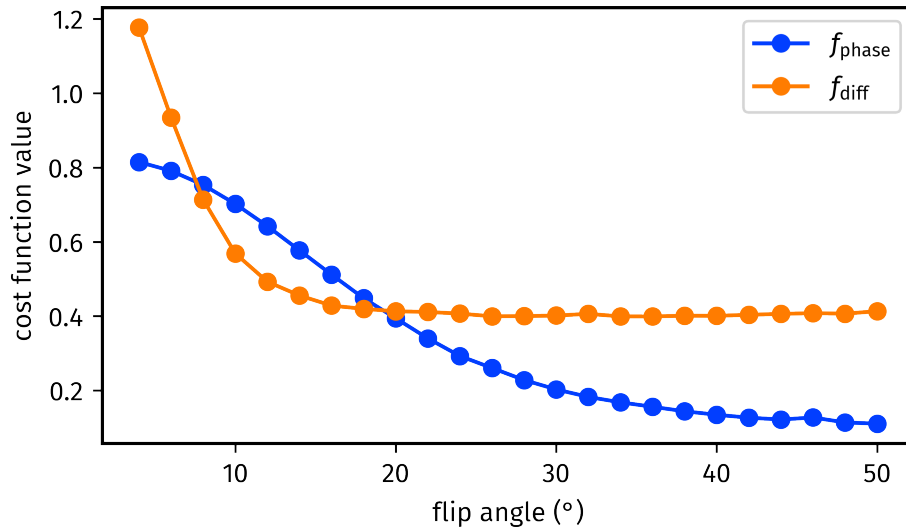
Figure 2.10: Behaviour of the two cost functions, f_{phase} and f_{diff}, on experimental pure shift spin echo spectra. *Data code:* 6C-190907.

2.4.3   Waveform parameterisation and optimisation

Given that a working optimisation setup, including cost functions, had been developed, it was a logical step to then test it out on a more challenging problem: namely, how the waveform used in the PSYCHE PSE could be modified. This goes beyond simply modifying the number of saltires, as was done in § 2.3. There is no real reason why the pulse *must* be an integer number of saltires: in principle it can have *any* shape, although being symmetric about the centre of the pulse would likely still be beneficial in terms of preserving the mechanism of spatiotemporal averaging.

A naive attempt at optimising the pulse would simply involve modifying every pulse point in the double-saltire waveform used in the PSYCHE element. As described in § 1.2, each pulse point consists of a pair of x- and y-amplitudes (c_x, c_y); therefore, for a pulse with n points, we would have a parameter vector $\mathbf{x} \in \mathbb{R}^{2n}$. Unfortunately, for PSYCHE, n is on the order of 10000, and an optimisation with 20000 points is totally unfeasible.*

As a result of this, we must consider other ways of parameterising the waveform. Several approaches to this issue have surfaced in the literature, such as the use of Fourier series,[36,69] Gaussian cascades,[70] or spline interpolation between a subset of pulse points.[71] In this instance, we can use the knowledge that the PSYCHE PSE is composed of saltire pulses to our advantage.

---

*Although problems of this size have been tackled using optimal control theory,[65–68] it is not really feasible to use it in cases where the pulse is applied *together* with a gradient, as is the case in PSYCHE. On top of that, the coupling networks and spin systems of interest are rather more complicated than in typical applications of optimal control.

Each saltire pulse is a linear combination of two chirps, defined by:

$$\phi(t) = \phi_0 + \pi\tau_{\mathrm{p}}(\Delta F)\left(\frac{t}{\tau_{\mathrm{p}}} - \frac{1}{2}\right)^2 \tag{2.29}$$ {eq:chirp_pulse_phase}

$$c_x(t) = f_{\mathrm{smooth}}(t)A\cos[\phi(t)] \tag{2.30}$$ {eq:chirp_pulse_cx}

$$c_y(t) = f_{\mathrm{smooth}}(t)A\sin[\phi(t)] \tag{2.31}$$ {eq:chirp_pulse_cy}

for $t \in [0, \tau_{\mathrm{p}}]$. Here, τ_{p} is the duration of the chirp, A is the amplitude of the chirp (which is time-independent), ϕ_0 the phase of the chirp, and ΔF the bandwidth. Equations (2.30) and (2.31) are identical to eq. (1.29), except for the addition of a *smoothing function* $f_{\mathrm{sm}}(t)$, which prevents large jumps in RF amplitude at the beginning and end of the pulse. f_{sm} depends on a smoothing parameter s_{sm}, which is typically 0.1–0.2:

$$f_{\mathrm{sm}}(t) = \begin{cases} \sin\left(\dfrac{\pi t'}{2s_{\mathrm{sm}}}\right) & 0 \leq t' < s_{\mathrm{sm}}; \\ 1 & s_{\mathrm{sm}} \leq t' < 1 - s_{\mathrm{sm}}; \\ \sin\left[\dfrac{\pi(1 - t')}{2s_{\mathrm{sm}}}\right] & s_{\mathrm{sm}} \leq t' \leq 1, \end{cases} \tag{2.32}$$ {eq:sming_function}

where $t' = t/\tau_{\mathrm{p}}$.

(could do with a figure here)

Given these expressions, and ignoring the smoothing function (which is only really described here for completeness) we see that there are four parameters of the chirp which can be modified: A, τ_{p}, ϕ_0, and ΔF. The two chirps which form one saltire pulse simultaneously sweep in opposite directions, which mean that ΔF for one chirp is the negative of the other; however, their parameters are otherwise equal.

We may, however, also envision a case where the pulse is constructed from two chirps which are applied at a different point in time, and also cover different bandwidths. This adds two more parameters to each chirp, namely t_0 (the starting time of the pulse) and f_0 (the centre of the pulse bandwidth). Each chirp therefore sweeps from the frequency $f_0 - (\Delta F)/2$ at a time t_0, to the frequency $f_0 + (\Delta F)/2$ at a time $t_0 + \tau_{\mathrm{p}}$. In total, this gives us six parameters per chirp which may be optimised: for a sum of two chirps, there are therefore 12 parameters in total. Since a sum of two chirps is not necessarily symmetric (with respect to reflection in time), I opted to reflect the waveform about its end, thus doubling the length of the pulse.

The initial point chosen was that corresponding to a *single* saltire after reflection:

- Chirp 1: $\tau_{\mathrm{p}} = 15\,\mathrm{ms}$; $\Delta F = -5\,\mathrm{kHz}$; $\phi_0 = 0$; $A = 36\,\mathrm{Hz}$; $t_0 = 0$; $f_0 = 5\,\mathrm{kHz}$;

- Chirp 2: $\tau_{\mathrm{p}} = 15\,\mathrm{ms}$; $\Delta F = 5\,\mathrm{kHz}$; $\phi_0 = 0$; $A = 36\,\mathrm{Hz}$; $t_0 = 0$; $f_0 = -5\,\mathrm{kHz}$;

Collectively, these two pulses sum up to become the *first half* of a single saltire with bandwidth 10 kHz. After reflection, the total duration of the saltire is 30 ms, and the amplitude is 72 Hz, which corresponds to a flip angle of approximately 32°.

Using this setup, several optimisations of the 12 parameters above were conducted. It was quickly noticed that, although f_{diff} was a better cost function than f_{phase}, this led to spurious optima being located. (FIGURE) The reason for this is almost certainly because the PSE distorts the relative intensity of signals: in particular, singlets have lower relative intensities than in the parent pulse–acquire spectrum. Of course, singlets are completely unimportant when devising a pure shift experiment. Furthermore, since singlets are typically more intense than the rest of the spectrum, they also contribute disproportionately to the cost function.

A simple and effective way to avoid this is to evaluate the cost function only on a specific part of the spectrum. In this case, I chose to use the H^α region between 4.72 and 5.94 ppm

(figure – spurious optima are gone, we have a `chirpopt_spurious.py` file)

(even with this, often converged to saltire... on the occasion something better than a saltire was found, typically the result is very close to that of a saltire — show TSE-PSYCHE spectrum obtained, 190831 AV600 cyclosporin)

While not quite as intractable as 20000 parameters, optimising a 12-parameter function clearly still proves to be a challenge. Although the cost functions described here do work, they are generally quite 'flat', in that they do not discriminate very sharply between 'good' and 'bad' spectra. Combined with the fact that the cost function is noisy, this makes experimental optimisation of the waveform an uphill task. With that said, much of the knowledge (and code) in this section was later used in the development of POISE. In particular, PSYCHE optimisations also ended up being part of POISE (§ 3.3.8).

2.5 Time-reversal method

sec:pureshift__timerev

This is basically the report which we sent to Gareth Morris (and was subsequently circulated amongst lots of people…). The conclusion was that it's got sensitivity which is comparable to PSYCHE but the artefact cancellation was very poor.

2.6 'Discrete PSYCHE'

sec:pureshift__dpsyche

More recent work mostly involving simulations.

2.7   Ultrafast PSYCHE-iDOSY

ec:pureshift__epsidosy

Collaborative stuff with Jean-Nicolas Dumez which never quite went anywhere (sadly)—although at EUROMAR, JND told me he now had a student (or a postdoc?) working on it and that they might send us some stuff.

2.8   References

Zangger2015PNMRS   (1)   Zangger, K. Pure shift NMR. *Prog. Nucl. Magn. Reson. Spectrosc.* **2015**, *86-87*, 1–20, DOI: `10.1016/j.pnmrs.2015.02.002`.

Castanar2017MRC   (2)   Castañar, L. Pure shift ^{1}H NMR: what is next? *Magn. Reson. Chem.* **2017**, *55*, 47–53, DOI: `10.1002/mrc.4545`.

Foroozandeh2014ACIE   (3)   Foroozandeh, M.; Adams, R. W.; Meharry, N. J.; Jeannerat, D.; Nilsson, M.; Morris, G. A. Ultrahigh-Resolution NMR Spectroscopy. *Angew. Chem., Int. Ed.* **2014**, *53*, 6990–6992, DOI: `10.1002/anie.201404111`.

Foroozandeh2018CEJ   (4)   Foroozandeh, M.; Morris, G. A.; Nilsson, M. PSYCHE Pure Shift NMR Spectroscopy. *Chem. Eur. J.* **2018**, *24*, 13988–14000, DOI: `10.1002/chem.201800524`.

Keeler2010   (5)   Keeler, J., *Understanding NMR Spectroscopy*, 2nd ed.; Wiley: Chichester, U.K., 2010.

Thrippleton2005JMR   (6)   Thrippleton, M. J.; Edden, R. A. E.; Keeler, J. Suppression of strong coupling artefacts in J-spectra. *J. Magn. Reson.* **2005**, *174*, 97–109, DOI: `10.1016/j.jmr.2005.01.012`.

Griesinger1986JCP   (7)   Griesinger, C.; Sørensen, O. W.; Ernst, R. R. Correlation of connected transitions by two-dimensional NMR spectroscopy. *J. Chem. Phys.* **1986**, *85*, 6837–6852, DOI: `10.1063/1.451421`.

Aue1976JCP   (8)   Aue, W. P.; Karhan, J.; Ernst, R. R. Homonuclear broad band decoupling and two-dimensional J-resolved NMR spectroscopy. *J. Chem. Phys.* **1976**, *64*, 4226–4227, DOI: `10.1063/1.431994`.

Xu1991JMR   (9)   Xu, P.; Wu, X.-L.; Freeman, R. Broadband-decoupled proton spectroscopy. *J. Magn. Reson.* **1991**, *95*, 132–148, DOI: `10.1016/0022-2364(91)90329-r`.

Nuzillard1996JMRSA   (10)   Nuzillard, J.-M. Time-Reversal of NMR Signals by Linear Prediction. Application to Phase-Sensitive Homonuclear J-Resolved Spectroscopy. *J. Magn. Reson., Ser. A* **1996**, *118*, 132–135, DOI: `10.1006/jmra.1996.0020`.

Simova1997JMR   (11)   Simova, S.; Sengstschmid, H.; Freeman, R. Proton Chemical-Shift Spectra. *J. Magn. Reson.* **1997**, *124*, 104–121, DOI: `10.1006/jmre.1996.1001`.

Pell2007JMR   (12)   Pell, A. J.; Keeler, J. Two-dimensional J-spectra with absorption-mode lineshapes. *J. Magn. Reson.* **2007**, *189*, 293–299, DOI: `10.1016/j.jmr.2007.09.002`.

Foroozandeh2015CC (13) Foroozandeh, M.; Adams, R. W.; Kiraly, P.; Nilsson, M.; Morris, G. A. Measuring couplings in crowded NMR spectra: pure shift NMR with multiplet analysis. *Chem. Commun.* **2015**, *51*, 15410–15413, DOI: [10.1039/c5cc06293d](10.1039/c5cc06293d).

Griesinger1985JACS (14) Griesinger, C.; Soerensen, O. W.; Ernst, R. R. Two-dimensional correlation of connected NMR transitions. *J. Am. Chem. Soc.* **1985**, *107*, 6394–6396, DOI: [10.1021/ja00308a042](10.1021/ja00308a042).

Sorensen1985JACS (15) Sørensen, O. W.; Griesinger, C.; Ernst, R. R. Time reversal of the evolution under scalar spin-spin interactions in NMR. Application for ω_1 decoupling in two-dimensional NOE spectroscopy. *J. Am. Chem. Soc.* **1985**, *107*, 7778–7779, DOI: [10.1021/ja00311a101](10.1021/ja00311a101).

Oschkinat1986JMR (16) Oschkinat, H.; Pastore, A.; Pfändler, P.; Bodenhausen, G. Two-dimensional correlation of directly and remotely connected transitions by z-filtered COSY. *J. Magn. Reson.* **1986**, *69*, 559–566, DOI: [10.1016/0022-2364(86)90176-9](10.1016/0022-2364(86)90176-9).

Pell2007MRC (17) Pell, A. J.; Edden, R. A. E.; Keeler, J. Broadband proton-decoupled proton spectra. *Magn. Reson. Chem.* **2007**, *45*, 296–316, DOI: [10.1002/mrc.1966](10.1002/mrc.1966).

Moutzouri2020ACIE (18) Moutzouri, P.; Paruzzo, F. M.; Simões de Almeida, B.; Stevanato, G.; Emsley, L. Homonuclear Decoupling in ^{1}H⊠NMR of Solids by Remote Correlation. *Angew. Chem., Int. Ed.* **2020**, *59*, 6235–6238, DOI: 10.1002/anie.201916335.

Bruschweiler2004JCP (19) Brüschweiler, R.; Zhang, F. Covariance nuclear magnetic resonance spectroscopy. *J. Chem. Phys.* **2004**, *120*, 5253–5260, DOI: [10.1063/1.1647054](10.1063/1.1647054).

Zhang2004JACS (20) Zhang, F.; Brüschweiler, R. Indirect Covariance NMR Spectroscopy. *J. Am. Chem. Soc.* **2004**, *126*, 13180–13181, DOI: [10.1021/ja047241h](10.1021/ja047241h).

Jaeger2014ARNMRS (21) Jaeger, M.; Aspers, R. L. E. G. Covariance NMR and Small Molecule Applications. *Annu. Rep. NMR Spectrosc.* **2014**, *83*, 271–349, DOI: [10.1016/B978-0-12-800183-7.00005-8](10.1016/B978-0-12-800183-7.00005-8).

Morris2010JACS (22) Morris, G. A.; Aguilar, J. A.; Evans, R.; Haiber, S.; Nilsson, M. True Chemical Shift Correlation Maps: A TOCSY Experiment with Pure Shifts in Both Dimensions. *J. Am. Chem. Soc.* **2010**, *132*, 12770–12772, DOI: [10.1021/ja1039715](10.1021/ja1039715).

Aguilar2012ACIE (23) Aguilar, J. A.; Colbourne, A. A.; Cassani, J.; Nilsson, M.; Morris, G. A. Decoupling Two-Dimensional NMR Spectroscopy in Both Dimensions: Pure Shift NOESY and COSY. *Angew. Chem., Int. Ed.* **2012**, *51*, 6460–6463, DOI: 10.1002/anie.201108888.

Foroozandeh2014JACS (24) Foroozandeh, M.; Adams, R. W.; Nilsson, M.; Morris, G. A. Ultrahigh-Resolution Total Correlation NMR Spectroscopy. *J. Am. Chem. Soc.* **2014**, *136*, 11867–11869, DOI: [10.1021/ja507201t](10.1021/ja507201t).

Lupulescu2012JMR (25) Lupulescu, A.; Olsen, G. L.; Frydman, L. Toward single-shot pure-shift solution ^{1}H NMR by trains of BIRD-based homonuclear decoupling. *J. Magn. Reson.* **2012**, *218*, 141–146, DOI: [10.1016/j.jmr.2012.02.018](10.1016/j.jmr.2012.02.018).

Meyer2013ACIE (26) Meyer, N. H.; Zangger, K. Simplifying Proton NMR Spectra by Instant Homonuclear Broadband Decoupling. *Angew. Chem., Int. Ed.* **2013**, *52*, 7143–7146, DOI: 10.1002/anie.201300129.

Kiraly2018MRC   (27)   Kiraly, P.; Nilsson, M.; Morris, G. A. Practical aspects of real-time pure shift HSQC experiments. *Magn. Reson. Chem.* **2018**, *56*, 993–1005, DOI: 10.1002/mrc.4704.

Donovan2014ACIE   (28)   Donovan, K. J.; Frydman, L. HyperBIRD: A Sensitivity-Enhanced Approach to Collecting Homonuclear-Decoupled Proton NMR Spectra. *Angew. Chem., Int. Ed.* **2014**, n/a–n/a, DOI: 10.1002/anie.201407869.

Taylor2021MRC   (29)   Taylor, D. A.; Natrajan, L. S.; Nilsson, M.; Adams, R. W. SABRE-enhanced real-time pure shift NMR spectroscopy. *Magn. Reson. Chem.* **2021**, *59*, 1244–1252, DOI: 10.1002/mrc.5206.

Aguilar2010ACIE   (30)   Aguilar, J. A.; Faulkner, S.; Nilsson, M.; Morris, G. A. Pure Shift ^{1}H NMR: A Resolution of the Resolution Problem? *Angew. Chem., Int. Ed.* **2010**, *49*, 3901–3903, DOI: 10.1002/anie.201001107.

Moutzouri2017CC   (31)   Moutzouri, P.; Chen, Y.; Foroozandeh, M.; Kiraly, P.; Phillips, A. R.; Coombes, S. R.; Nilsson, M.; Morris, G. A. Ultraclean pure shift NMR. *Chem. Commun.* **2017**, *53*, 10188–10191, DOI: 10.1039/c7cc04423b.

Zangger1997JMR   (32)   Zangger, K.; Sterk, H. Homonuclear Broadband-Decoupled NMR Spectra. *J. Magn. Reson.* **1997**, *124*, 486–489, DOI: 10.1006/jmre.1996.1063.

Garbow1982CPL   (33)   Garbow, J. R.; Weitekamp, D. P.; Pines, A. Bilinear rotation decoupling of homonuclear scalar interactions. *Chem. Phys. Lett.* **1982**, *93*, 504–509, DOI: 10.1016/0009-2614(82)83229-6.

Aguilar2011ACIE   (34)   Aguilar, J. A.; Nilsson, M.; Morris, G. A. Simple Proton Spectra from Complex Spin Systems: Pure Shift NMR Spectroscopy Using BIRD. *Angew. Chem., Int. Ed.* **2011**, *50*, 9716–9717, DOI: 10.1002/anie.201103789.

Foroozandeh2020JMR   (35)   Foroozandeh, M. Spin dynamics during chirped pulses: applications to homonuclear decoupling and broadband excitation. *J. Magn. Reson.* **2020**, *318*, 106768, DOI: 10.1016/j.jmr.2020.106768.

Kupce1995JMRSB   (36)   Kupce, E.; Boyd, J.; Campbell, I. D. Short Selective Pulses for Biochemical Applications. *J. Magn. Reson., Ser. B* **1995**, *106*, 300–303, DOI: 10.1006/jmrb.1995.1049.

Giraud2010ACIE   (37)   Giraud, N.; Béguin, L.; Courtieu, J.; Merlet, D. Nuclear Magnetic Resonance Using a Spatial Frequency Encoding: Application to J-Edited Spectroscopy along the Sample. *Angew. Chem., Int. Ed.* **2010**, *49*, 3481–3484, DOI: 10.1002/anie.200907103.

Gubensak2014CC   (38)   Gubensäk, N.; Fabian, W. M. F.; Zangger, K. Disentangling scalar coupling patterns by real-time SERF NMR. *Chem. Commun.* **2014**, *50*, 12254–12257, DOI: 10.1039/c4cc05892e.

Mishra2017JMR   (39)   Mishra, S. K.; Suryaprakash, N. Pure shift edited ultra high resolution NMR spectrum with complete eradication of axial peaks and unwanted couplings. *J. Magn. Reson.* **2017**, *279*, 74–80, DOI: 10.1016/j.jmr.2017.04.014.

Buchberger2018MRC (40) Buchberger, K.; Walenta, M.; Zangger, K. Extracting unresolved coupling constants from complex multiplets by a real-time J-upscaled SERF experiment. *Magn. Reson. Chem.* **2018**, *56*, 934–940, DOI: `10.1002/mrc.4699`.

Uhrin1993JMRSA (41) Uhrin, D.; Liptaj, T.; Kover, K. E. Modified BIRD Pulses and Design of Heteronuclear Pulse Sequences. *J. Magn. Reson., Ser. A* **1993**, *101*, 41–46, DOI: `10.1006/jmra.1993.1005`.

Sakhaii2009JMR (42) Sakhaii, P.; Haase, B.; Bermel, W. Experimental access to HSQC spectra decoupled in all frequency dimensions. *J. Magn. Reson.* **2009**, *199*, 192–198, DOI: `10.1016/j.jmr.2009 .04.016`.

Paudel2013ACIE (43) Paudel, L.; Adams, R. W.; Király, P.; Aguilar, J. A.; Foroozandeh, M.; Cliff, M. J.; Nilsson, M.; Sándor, P.; Waltho, J. P.; Morris, G. A. Simultaneously Enhancing Spectral Resolution and Sensitivity in Heteronuclear Correlation NMR Spectroscopy. *Angew. Chem., Int. Ed.* **2013**, *52*, 11616–11619, DOI: `10.1002/anie.201305709`.

Reinsperger2014JMR (44) Reinsperger, T.; Luy, B. Homonuclear BIRD-decoupled spectra for measuring one-bond couplings with highest resolution: CLIP/CLAP-RESET and constant-time-CLIP/CLAP-RESET. *J. Magn. Reson.* **2014**, *239*, 110–120, DOI: `10.1016/j.jmr.2013.11.015`.

Nolis2019JMR_psHSQC (45) Nolis, P.; Motiram-Corral, K.; Pérez-Trujillo, M.; Parella, T. Broadband homodecoupled time-shared ^{1}H–^{13}C and ^{1}H–^{15}N HSQC experiments. *J. Magn. Reson.* **2019**, *298*, 23–30, DOI: `10.1016/j.jmr.2018.11.005`.

Singh2020JMR (46) Singh, U.; Bhattacharya, S.; Baishya, B. Pure shift HMQC: Resolution and sensitivity enhancement by bilinear rotation decoupling in the indirect and direct dimensions. *J. Magn. Reson.* **2020**, *311*, 106684, DOI: `10.1016/j.jmr.2020.106684`.

Zwahlen1997JACS (47) Zwahlen, C.; Legault, P.; Vincent, S. J. F.; Greenblatt, J.; Konrat, R.; Kay, L. E. Methods for Measurement of Intermolecular NOEs by Multinuclear NMR Spectroscopy: Application to a Bacteriophage λ N-Peptide/boxBRNA Complex. *J. Am. Chem. Soc.* **1997**, *119*, 6711–6721, DOI: `10.1021/ja970224q`.

Kupce2007JMR (48) Kupče, E.; Freeman, R. Compensated adiabatic inversion pulses: Broadband INEPT and HSQC. *J. Magn. Reson.* **2007**, *187*, 258–265, DOI: `10.1016/j.jmr.2007.05.009`.

Thrippleton2003ACIE (49) Thrippleton, M. J.; Keeler, J. Elimination of Zero-Quantum Interference in Two-Dimensional NMR Spectra. *Angew. Chem., Int. Ed.* **2003**, *42*, 3938–3941, DOI: `10.1002/anie.2 00351947`.

Timari2015CEJ (50) Timári, I.; Szilágyi, L.; Kövér, K. E. PSYCHE CPMG–HSQMBC: An NMR Spectroscopic Method for Precise and Simple Measurement of Long-Range Heteronuclear Coupling Constants. *Chem. Eur. J.* **2015**, *21*, 13939–13942, DOI: `10.1002/chem.201502641`.

Koos2016ACIE (51) Koos, M. R. M.; Kummerlöwe, G.; Kaltschnee, L.; Thiele, C. M.; Luy, B. CLIP-COSY: A Clean In-Phase Experiment for the Rapid Acquisition of COSY-type Correlations. *Angew. Chem., Int. Ed.* **2016**, *55*, 7655–7659, DOI: `10.1002/anie.201510938`.

Sinnaeve2016ACIE   (52)   Sinnaeve, D.; Foroozandeh, M.; Nilsson, M.; Morris, G. A. A General Method for Extracting Individual Coupling Constants from Crowded ^{1}H NMR Spectra. *Angew. Chem., Int. Ed.* **2016**, *55*, 1090–1093, DOI: `10.1002/anie.201508691`.

Aguilar2018MRC   (53)   Aguilar, J. A.; Belda, R.; Gaunt, B. R.; Kenwright, A. M.; Kuprov, I. Separating the coherence transfer from chemical shift evolution in high-resolution pure shift COSY NMR. *Magn. Reson. Chem.* **2018**, *56*, 969–975, DOI: `10.1002/mrc.4727`.

Kaltschnee2016JMR   (54)   Kaltschnee, L.; Knoll, K.; Schmidts, V.; Adams, R. W.; Nilsson, M.; Morris, G. A.; Thiele, C. M. Extraction of distance restraints from pure shift NOE experiments. *J. Magn. Reson.* **2016**, *271*, 99–109, DOI: `10.1016/j.jmr.2016.08.007`.

Ilgen2021JMR   (55)   Ilgen, J.; Nowag, J.; Kaltschnee, L.; Schmidts, V.; Thiele, C. M. Gradient selected pure shift EASY-ROESY techniques facilitate the quantitative measurement of 1H,1H-distance restraints in congested spectral regions. *J. Magn. Reson.* **2021**, *324*, 106900, DOI: `10.1016/j.jmr.2020.106900`.

Foroozandeh2016ACIE   (56)   Foroozandeh, M.; Castañar, L.; Martins, L. G.; Sinnaeve, D.; Poggetto, G. D.; Tormena, C. F.; Adams, R. W.; Morris, G. A.; Nilsson, M. Ultrahigh-Resolution Diffusion-Ordered Spectroscopy. *Angew. Chem. Int. Ed.* **2016**, *55*, 15579–15582, DOI: `10.1002/anie.201609676`.

Frydman2002PNASUSA   (57)   Frydman, L.; Scherf, T.; Lupulescu, A. The acquisition of multidimensional NMR spectra within a single scan. *Proc. Natl. Acad. Sci. U. S. A.* **2002**, *99*, 15858–15862, DOI: `10.1073/pnas.252644399`.

Pelupessy2003JACS   (58)   Pelupessy, P. Adiabatic Single Scan Two-Dimensional NMR Spectrocopy. *J. Am. Chem. Soc.* **2003**, *125*, 12345–12350, DOI: `10.1021/ja034958g`.

Frydman2003JACS   (59)   Frydman, L.; Lupulescu, A.; Scherf, T. Principles and Features of Single-Scan Two-Dimensional NMR Spectroscopy. *J. Am. Chem. Soc.* **2003**, *125*, 9204–9217, DOI: `10.1021/ja030055b`.

Kiraly2021ACIE   (60)   Kiraly, P.; Kern, N.; Plesniak, M. P.; Nilsson, M.; Procter, D. J.; Morris, G. A.; Adams, R. W. Single-Scan Selective Excitation of Individual NMR Signals in Overlapping Multiplets. *Angew. Chem., Int. Ed.* **2021**, *60*, 666–669, DOI: `10.1002/anie.202011642`.

Dumez2018PNMRS   (61)   Dumez, J.-N. Spatial encoding and spatial selection methods in high-resolution NMR spectroscopy. *Prog. Nucl. Magn. Reson. Spectrosc.* **2018**, *109*, 101–134, DOI: `10.1016/j.pnmrs.2018.08.001`.

Nelder1965TCJ   (62)   Nelder, J. A.; Mead, R. A Simplex Method for Function Minimization. *The Computer Journal* **1965**, *7*, 308–313, DOI: `10.1093/comjnl/7.4.308`.

McKinnon1998SIAMJO   (63)   McKinnon, K. I. M. Convergence of the Nelder–Mead Simplex Method to a Nonstationary Point. *SIAM J. Optim.* **1998**, *9*, 148–158, DOI: `10.1137/s1052623496303482`.

Hogben2011JMR   (64)   Hogben, H. J.; Krzystyniak, M.; Charnock, G. T. P.; Hore, P. J.; Kuprov, I. Spinach – A software library for simulation of spin dynamics in large spin systems. *J. Magn. Reson.* **2011**, *208*, 179–194, DOI: `10.1016/j.jmr.2010.11.008`.

Khaneja2005JMR   (65)   Khaneja, N.; Reiss, T.; Kehlet, C.; Schulte-Herbrüggen, T.; Glaser, S. J. Optimal control of coupled spin dynamics: design of NMR pulse sequences by gradient ascent algorithms. *J. Magn. Reson.* **2005**, *172*, 296–305, DOI: `10.1016/j.jmr.2004.11.004`.

deFouquieres2011JMR   (66)   De Fouquieres, P.; Schirmer, S. G.; Glaser, S. J.; Kuprov, I. Second order gradient ascent pulse engineering. *J. Magn. Reson.* **2011**, *212*, 412–417, DOI: `10.1016/j.jmr.2011.07.023`.

Glaser2015EPJD   (67)   Glaser, S. J.; Boscain, U.; Calarco, T.; Koch, C. P.; Köckenberger, W.; Kosloff, R.; Kuprov, I.; Luy, B.; Schirmer, S.; Schulte-Herbrüggen, T.; Sugny, D.; Wilhelm, F. K. Training Schrödinger's cat: quantum optimal control. *Eur. Phys. J. D* **2015**, *69*, No. 279, DOI: `10.1140/epjd/e2015-60464-1`.

Goodwin2016JCP   (68)   Goodwin, D. L.; Kuprov, I. Modified Newton-Raphson GRAPE methods for optimal control of spin systems. *J. Chem. Phys.* **2016**, *144*, 204107, DOI: `10.1063/1.4949534`.

Geen1991JMR   (69)   Geen, H.; Freeman, R. Band-selective radiofrequency pulses. *J. Magn. Reson.* **1991**, *93*, 93–141, DOI: `10.1016/0022-2364(91)90034-q`.

Emsley1990CPL   (70)   Emsley, L.; Bodenhausen, G. Gaussian pulse cascades: New analytical functions for rectangular selective inversion and in-phase excitation in NMR. *Chem. Phys. Lett.* **1990**, *165*, 469–476, DOI: `10.1016/0009-2614(90)87025-m`.

Ewing1990CP   (71)   Ewing, B.; Glaser, S. J.; Drobny, G. P. Development and optimization of shaped NMR pulses for the study of coupled spin systems. *Chem. Phys.* **1990**, *147*, 121–129, DOI: `10.1016/0301-0104(90)85028-u`.

refsection:3

refsection:4

List of figures

List of tables